Journal of Materials Chemistry A

Copper Manganese Oxide Enhanced Nanoarray-Based Monolithic Catalysts for Hydrocarbon Oxidation

Journal:	*Journal of Materials Chemistry A*
Manuscript ID	TA-ART-07-2018-006459.R1
Article Type:	Paper
Date Submitted by the Author:	07-Sep-2018
Complete List of Authors:	Chen, Sheng-Yu; University of Connecticut, Department of Chemistry Tang, Wenxiang; Intitute of Materials Sicence, University of Connecticut He, Junkai; University of Connecticut, Institute of Materials Science Miao, Ran; University of Connecticut, Department of Chemistry Lin, Hui-Jan; Institute of Materials Science, Department of Materials Science and Engineering Song, Wenqiao; University of Connecticut, Department of Chemistry Wang, Sibo; University of Connecticut, Institute of Materials Science Gao, Pu-Xian; University of Connecticut, Suib, Steven; University of Connecticut, U-60, Department of Chemistry

Journal Name

ARTICLE

Copper Manganese Oxide Enhanced Nanoarray-Based Monolithic Catalysts for Hydrocarbon Oxidation

Received 00th January 20xx,
Accepted 00th January 20xx

DOI: 10.1039/x0xx00000x

www.rsc.org/

Sheng-Yu Chen,[a] Wenxiang Tang,[b] Junkai He,[b] Ran Miao,[a] Hui-Jan Lin,[a] Wenqiao Song,[a] Sibo Wang,[b] Pu-Xian Gao,*[,b] and Steven L. Suib*[,a,b]

Copper manganese oxide ($CuMn_2O_4$) was introduced into the nanoarray-based monolithic catalysts system for advanced exhaust after-treatment. Through scalable and cost-effective hydrothermal reactions, nanosheet layers of copper manganese oxide were uniformly coated onto the manganese oxide nanoarrays (HM-PCR), which were grown on the cordierite honeycomb monoliths. The core nanoarray support, HM-PCR, a well-defined array architecture for active material deposition, contributed to an increase of open surface area and thus enhanced catalytic oxidation performance. The $CuMn_2O_4$ coated nanoarray-based catalyst, NA-$CuMn_2O_4$, shows efficient 90% propane (C_3H_8) conversion at around 400 °C, which is 50 °C and 75 °C lower than $CuMn_2O_4$ wash-coated catalyst (WC-$CuMn_2O_4$) and Pd loaded catalyst (WC-Pd), respectively. Compared to monolithic catalysts with a traditional alumina support, the benefit of nanoarray morphology was demonstrated by correlating the variation of surface area to the reactivity. The incorporation of cobalt ions was found to increase the specific surface area and thus enhance C_3H_8 conversion of $CuMn_2O_4$. The $CuMn_2O_4/MnO_2$ nanoarray-based monoliths are promising types of emission control devices.

1. Introduction

Air pollution is a long-term issue that has constantly deteriorated the global atmospheric quality and human health in the past.[1] The rapidly decayed air quality urges ever-tightened regulations by global legislatures for emissions control.[2] This also challenges the automotive industry to develop more efficient catalysts for after-treatment of various emissions, such as carbon monoxide (CO), nitrogen oxides (NO_x), sulfur oxides (SO_x), and hydrocarbons (HCs).[3] Meanwhile, state-of-the-art platinum-group metal (PGM)-based (e.g. Pd, Pt, Rh) catalytic converters face challenges for a balance between catalytic efficiency and material cost.[4-7] Introducing transition metal oxides (e.g. Co_3O_4, MnO_2, CuO, and CeO_2) is a cost-effective strategy to improve catalytic converters with enhanced surface area, porosity, reactivity, and thermal stability.[8-11] Perovskite materials also showed some outstanding catalytic performance with positive synergy with noble metals.[12-14]

Recently, nanoarray-based monolithic catalysts have attracted great interest in gas phase catalysis and detection.[15-19] A new type of monolithic catalysts with hierarchical nanoarray structures was invented by Gao and co-workers. Different from conventional wash-coated catalytic converters, transition metal oxide nanoarrays (e.g. ZnO, Co_3O_4, and TiO_2) were in situ grown on bare ceramic cordierite ($2MgO{\cdot}2Al_2O_3{\cdot}5SiO_2$) honeycomb monoliths.[20-24] Compared to the wash-coating method, this new configuration exhibited unique characteristics as a result of the nanoarray architectures. Firstly, the usually vertically-aligned nanoarrays on honeycomb channel surfaces provide open surfaces for more efficient molecular diffusion and improve heterogeneous interactions.[25] Secondly, micron-thick nanoarrays replace tens to hundred-microns thick porous alumina powder layer as supports, significantly reducing material usage and weight of monolithic catalysts.[20] Thirdly, uniform nanoarray coatings with thin thickness (1-10 μm) inside honeycomb channels further reduced the pressure-drop (Fig. S1).[25] Finally, the well-bound nanostructures with well-defined surfaces on the substrate surface not only improve the catalytic performance, but also prevent or mitigate the agglomeration of nanoparticles.[26] These beneficial characteristics have enabled these transition metal oxide nanoarray integrated monolithic catalysts as a promising class of new catalytic converters superior to the currently wash-coated commercial ones.

Previously, manganese oxide (MnO_2) based nanoarrays have been fabricated on honeycomb monoliths by a hydrothermal synthesis method.[27] Compared to other transition metal oxides such as ZnO and Co_3O_4, MnO_2 nanoarray based monolithic catalysts feature various merits such as high robustness, low cost, good acidic tolerance, low toxicity, and no need of pre-seeding, demonstrating their good

[a] Department of Chemistry, U-3060, University of Connecticut, Storrs, Connecticut 06269-3060, USA
[b] Department of Materials Science and Engineering & Institute of Materials Science, U-3136, University of Connecticut, Storrs, Connecticut 06269-3136, USA

† Footnotes relating to the title and/or authors should appear here.
Electronic Supplementary Information (ESI) available: [details of any supplementary information available should be included here]. See DOI: 10.1039/x0xx00000x

potential for heterogeneous catalysis. However, the catalytic activity of MnO_2 is usually lowered when well-crystallized nanoarrays are formed. Therefore, combing additional highly active material to enhance the activity of MnO_2 nanoarrays is a major challenge.

In industry, copper-manganese mixed oxides have been widely projected as promising heterogeneous catalysts with remarkable reactivity for CO, NO_x, and hydrocarbons (HCs) at low temperature and cheap cost for several decades, but the detailed mechanism of catalysis still needs more future investigations.[28-31] The reactivity of copper manganese oxide varies with several factors such as elemental composition, crystal structure, calcination temperature, surface area, and aging.[28, 32-34] Among the various copper manganese oxides, amorphous copper-manganese oxide is commonly considered as the most active one. Veprek et al. showed Cu^{2+} and Mn^{3+} as dominant active sites in both active and plasma reoxidized catalysts, which might contribute to the high reactivity.[35] During the catalytic process, thermal effects usually cause conversion of amorphous copper-manganese oxides into Hopcalite ($CuMn_2O_4$), a spinel structure with a general formula of AB_2O_4, with partial activity loss.[36] According to the resonance system proposed by Fortunato et al. and Cocke et al., $Cu^{2+} + Mn^{3+} \leftrightarrow Cu^{+} + Mn^{4+}$, the co-existence of Cu and Mn species retain some activity of hopcalite catalysts.[37, 38] Specifically, Cu^{2+}/Mn^{4+} and Cu^{1+}/Mn^{3+} promote the adsorption of CO and O_2, respectively. In addition, partial replacement of the tetrahedral sites in spinel AB_2O_4 by other transition metals (e.g., Co, Ni, Fe, and Au) might promote the catalytic performance by enhancing surface lattice oxygen mobility.[33, 39]

In this study, copper manganese oxide ($CuMn_2O_4$) and nanoarray architectures were combined to form $CuMn_2O_4$/nanoarray-based monolithic catalysts for propane (C_3H_8) oxidation. It is noted that, although Co-alloyed MnO_2 based nanoparticles have shown a promising 90% conversion for total propane oxidation at ~200 - 300 °C while adopting the high pressure-drop fixed bed reactor configuration,[40-42] the respective nanoarray-based monolithic catalysts display so far a 90% conversion temperature at a higher range of 300 - 400 °C. Here we utilize the previously reported manganese oxide nanoarray, HM-PCR, as the core,[27] and precipitate on top the $CuMn_2O_4$ and Co-doped $CuMn_2O_4$ nanocoating by mild hydrothermal reactions, denoted as NA-$CuMn_2O_4$, NA-$Co_{0.36}Cu_{0.64}Mn_2O_4$, and NA-$Co_{0.53}Cu_{0.47}Mn_2O_4$ based on the composition revealed by inductively coupled plasma-mass spectrometry (ICP-MS). All three catalysts possess $CuMn_2O_4$ based compositions with low crystallinity and high conversion of hydrocarbon oxidations. Incorporation of trace cobalt ions led to partial Cu replacement by Co, which was found to enhance reactivity at low temperature, with increased surface area but compromised thermal stability. To understand the catalytic contribution from nanoarray architectures, monolithic catalysts loaded with similar amounts of $CuMn_2O_4$ and $Co_xCu_{1-x}Mn_2O_4$ materials were prepared by a wash-coating method using alumina powder (α-Al_2O_3) as the support. An additional Pd-loaded catalyst was used as a reference to compare the high reactivity of our $CuMn_2O_4$ catalysts. Further studies of nitrogen isothermal adsorption, X-ray photoelectron spectroscopy (XPS), hydrogen temperature-programmed reduction (H_2-TPR), and oxygen temperature-programmed desorption (O_2-TPD) show how the increased surface area and lattice oxygen mobility correlate closely with catalytic performance of Co-doped $CuMn_2O_4$ catalysts.

2. Experimental section and synthesis

2.1 Synthesis of Catalysts

All chemicals in this study were purchased from chemical vendors without further purification. The cordierite honeycomb monolith substrates were obtained from Corning Corp. The cordierite substrate was sonicated in ethanol and water for 30 min and dried at 90 °C for 12 h before reaction.

The synthesis of core MnO_2 nanoarray, HM-PCR, followed previous work.[27] 15.2 g manganese sulfate monohydrate ($MnSO_4 \cdot H_2O$, 90 mmol) and 19.4 g potassium chlorate ($KClO_3$, 158 mmol) were dissolved in 300 mL Deionized (DI) water with 5 mL sulfuric acid. Then the solution was transferred into a 400 mL capped glass bottle with the cordierite substrate located on the bottom and heated at 90 °C in an oil bath with a mechanical stirrer from the top for 12 h (Fig. S2). The reactor was cooled down at room temperature for 2 h after the reaction was complete. Rinsing with water and drying in air were applied alternatively to remove the residual reagent inside the monolith channels. The monolithic catalysts were sonicated in water for 2 h to remove loose manganese oxide powder, then dried in a vacuum oven at 60 °C for overnight.

A layer of copper manganese oxide ($CuMn_2O_4$) was applied onto the core nanoarrays, HM-PCR, by a secondary hydrothermal reaction. 3.79 g potassium permanganate ($KMnO_4$, 24 mmol) and 2.89 g copper nitrate trihydrate ($Cu(NO_3)_2 \cdot 3H_2O$, 12 mmol) were dissolved in 60 mL DI water. The mixed solution was transferred to a 150 mL glass bottle within a nanoarray (HM-PCR) coated honeycomb monolithic substrates and heated at 90 °C in a water bath for 16 h. After the reaction, similar workup as the synthesis of HM-PCR was applied following the order, rinsing, sonication, and vacuum drying. For Co-doped catalysts, NA-$Co_{0.36}Cu_{0.64}Mn_2O_4$ and NA-$Co_{0.53}Cu_{0.47}Mn_2O_4$, 1% and 2% mole ratios with respect to the total reagent of cobalt nitrate hexahydrate ($Co(NO_3)_2 \cdot 6H_2O$) were added into the solution, respectively. All $CuMn_2O_4$ series of monolithic catalysts were calcined at 300 °C for 2 h under ambient condition.

$CuMn_2O_4$ and Co-doped $CuMn_2O_4$ powder collected from each hydrothermal reaction were loaded on cordierite substrates using wash-coating methods for comparison with nanoarray-based monolithic catalysts. Mixtures of 0.2 g $CuMn_2O_4$, 0.8 g α-Al_2O_3, and 5 mL DI water were stirred for 2 h to form a slurry with 20% active materials. For each wash-coating cycle, the cordierite substrate was dipped into the slurry for 30 min and blown by nitrogen flow to remove extra slurry. The wet cordierite substrate was dried at 150 °C for 1 h in an oven. The same procedure was repeated for 4 to 5 times

to obtain similar loading amounts of $CuMn_2O_4$ materials to nanoarray-based catalysts. Each wash-coated substrate was also calcined at 300 °C for 2 h before catalytic tests.

Following the same procedure given above, a commercial solution of 1% Pd/Al_2O_3 was used to prepare Pd wash-coated monolithic catalysts. The calculated Pd loading amount on cordierite substrates was 1 g/L. The Pd loaded monolithic catalysts were calcined at 500 °C for 2 h before the catalytic tests.

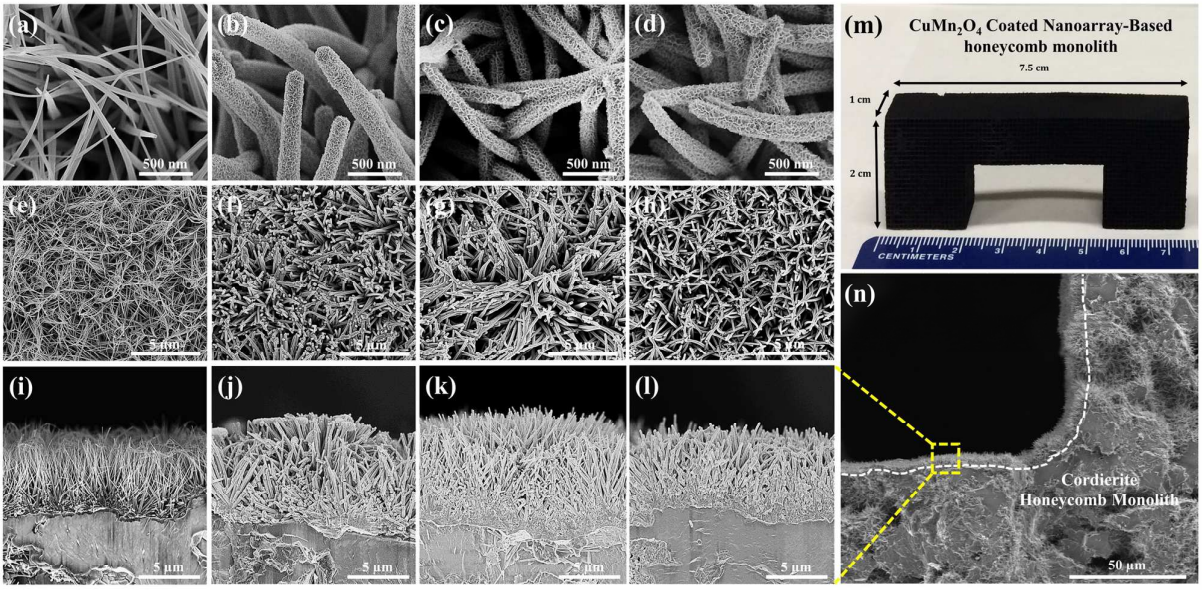

Fig. 1. SEM images of nanoarrays HM-PCR with and without $CuMn_2O_4$ coatings by on the cordierite substrate. Column (a) HM-PCR, (b) NA-$CuMn_2O_4$, (c) NA-$Co_{0.36}Cu_{0.64}Mn_2O_4$, and (d) NA-$Co_{0.53}Cu_{0.47}Mn_2O_4$. Upper and middle rows showed top-view images; lower row showed cross-section images. (m) The $CuMn_2O_4$ coated nanoarray-based honeycomb monolith. (n) The cross-section view of nanoarrays grown on a monolithic cordierite substrate around channel corners.

2.2 Materials Characterization

The powder X-ray diffraction (PXRD) analyses were conducted using a Rigaku Ultimate IV diffractometer (Cu Kα radiation, λ= 1.5406 Å) with an operating beam voltage of 40.0 KV and a beam current of 44 mA. The diffraction patterns were collected between a 2 θ range of 5 - 75°. The surface morphologies of all monolithic and powder samples were determined with a field emission scanning electron microscope (FE-SEM) FEI Nova NanoSEM 450 at an accelerating voltage of 2 kV. Transmission electron microscopy (TEM) images were obtained using a FEI Talos F200X with an accelerating voltage of 200 kV. The surface elemental analysis of catalysts was conducted with X-ray photoelectron spectroscopy (XPS) using a PHI Quantera SXM spectrometer with multi-probes and Al-K alpha radiation source

(λ= 1486.6 eV). For correction of surface charging, the binding energies in XPS spectra were calibrated using the signal from adventitious carbon (C 1s, 284.6 eV). The elemental analysis of transition metals in catalysts was tested by an Agilent 7900 ICP-MS.

The surface areas of monolithic and powder-form samples were measured with nitrogen adsorption-desorption experiments using a Quantachrome Autosorb-1-1C automated adsorption system and calculated with the Brunauer–Emmett–Teller (BET) method. Both nanoarray-based and wash-coated monolithic catalysts were degassed at 150 °C for 6 h to remove moisture and other physically adsorbed species. The experiments of N_2 isothermal adsorption were measured at relative pressures (P/P_0) from 0.005 to 0.995 then followed by desorption from 0.995 to 0.12.

Both hydrogen temperature programmed reduction (H_2-TPR) and oxygen temperature programmed desorption (O_2-TPD) tests were performed using a Micromeritics ChemiSorb 2720 flow gas analyzer coupled with a thermal conductivity detector (TCD). Each piece of monolithic samples with 7 × 7 channels in cross section (7 mm × 7 mm × 10 mm, W x H x L) was packed in a quartz tube and located in the attached programmable furnace. All monolithic samples were pretreated with a nitrogen flow (N_2, 20 SCCM) at 200 °C for 1 h to remove surface adsorbed moisture and impurities. 1% hydrogen (H_2) balanced by nitrogen (N_2) with 50 SCCM flow rate was used in the H_2-TPR experiments. For O_2-TPD experiments, pure oxygen was purged through samples with a 25 SCCM flow rate at 250 °C for 1 h to stabilize lattice oxygen populations of active materials. All temperature-programmed measurements were performed from room temperature to 600 °C with a ramping rate of 10°C/min.

The catalytic performances of all copper manganese oxide coated monolithic catalysts were evaluated by carbon monoxide (CO) and propane (C_3H_8) oxidations using a BenchCAT reactor (Altamira Instruments). A Dycor Dymaxion

mass spectrometer and an Agilent MicroGC were used for the analysis and quantification of gas species. For each catalytic test, one piece of the monolithic catalyst with 5 × 5 channels in cross section (5 mm × 5 mm × 10 mm, W x H x L) was packed in quartz tubing. The feed gas was 0.3% C_3H_8, 10% O_2 and balanced by N_2 with a 100 SCCM flow rate and 24,000 h^{-1} space velocity. A pretreatment under nitrogen was applied at 200 °C for 1 h before the catalytic tests to remove surface adsorbed moisture and impurities from the active materials.

3. Results

3.1 Structural and morphology, and surface area characterization

Fig. 1 shows the SEM images of core manganese oxide nanoarrays (HM-PCR) and copper manganese oxide coated nanoarrays fabricated on the cordierite honeycomb monoliths. As shown in the first column [(a), (e), and (i)], the HM-PCR nanoarrays have average lengths of ~ 5 µm and small diameters of ~ 50 nm. Through hydrothermal reactions, transition metal oxide layers of $CuMn_2O_4$, and Co-doped $CuMn_2O_4$ ($Co_{0.36}Cu_{0.64}Mn_2O_4$ and $Co_{0.53}Cu_{0.47}Mn_2O_4$) were coated uniformly on the HM-PCR nanoarrays while maintaining the array architectures, as revealed in Figs. 1(b)-(d) and Figs. 1(f)-(h). The cross-section SEM images shown in Figs. 1(j)-(l) reveal that the homogeneous $CuMn_2O_4$ coatings occur along each nanorod of HM-PCR nanoarrays from top to bottom. Figs. 1(m) and 1(n) present that the $CuMn_2O_4$ based nanoarrays were smoothly fabricated on the cordierite substrate even inside the channels of honeycomb monoliths, especially no coating aggregation around corner areas. The thickness of all coating layers is controllable by adjusting reaction conditions of hydrothermal synthesis, i.e. temperature, time, concentration, and Co amount. In general, the average thickness of $CuMn_2O_4$ coating can reach 100 nm with 16 h hydrothermal reaction, but only 4 h with addition of 1% Co and 1 h with 2% Co, respectively. Both core nanoarrays and $CuMn_2O_4$ coatings were stable on cordierite substrates without obvious detachment after 2 h of sonication in water.

X-ray diffraction (XRD) was conducted on the powders collected from each hydrothermal reaction to identify their crystal structures [Fig. 2(a)], because the intensities of the diffraction patterns from the cordierite substrate were much stronger than the diffraction patterns from the manganese oxide arrays, HM-PCR, and coating material, $CuMn_2O_4$. XRD patterns Fig. 2(a) revealed that the core nanoarrays grown on the cordierite substrates were indexed to the cryptomelane manganese oxide ($K_{2-x}Mn_8O_{16}$, tetragonal, $a = b = 9.82$ Å and $c = 2.85$ Å, JCPDS: 29-1020). In Fig. 2(a), The XRD patterns of coated copper manganese oxide materials displayed very low crystallinity and it was hard to identify the crystal structure, even after calcination at 400 °C.[30, 33] The XRD patterns of each catalyst calcined at temperatures from 300 to 500 °C are shown in Figs. 2(b)-(d). Fig. 2(b) shows that the pure $CuMn_2O_4$ coating layer was converted to the hopcalite structure (JCPDS: 74-2422) after calcination at 500 °C.[43] In Figs. 2(c) and 2(d),

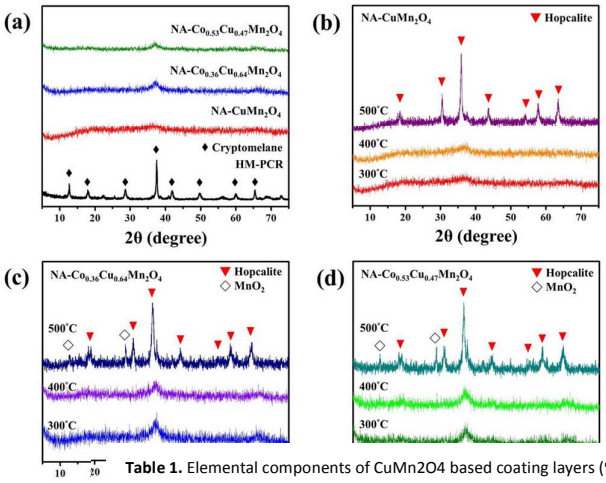

Fig. 2. (a) XRD
$Co_{0.36}Cu_{0.64}Mn_2$
(b) NA-$CuMn_2$
300, 400, and 5

Table 1. Elemental components of CuMn2O4 based coating layers (%)

	Mn	Cu	Co	Total
NA-$CuMn_2O_4$	64.9	35.1	-	100.0
NA-$Co_{0.36}Cu_{0.64}Mn_2O_4$	65.7	22.1	12.3	100.0
NA-$Co_{0.53}Cu_{0.47}Mn_2O_4$	64.0	16.9	19.2	100.0

The - entries signify not applicable or measured.

diffraction peaks around 13° and 29° can be observed and indexed to the (110) and (310) planes of α-MnO_2 (JCPDS: 44-0141), respectively, which indicates an additional phase segregation happened in the two Co-doped catalysts after high temperature calcination.

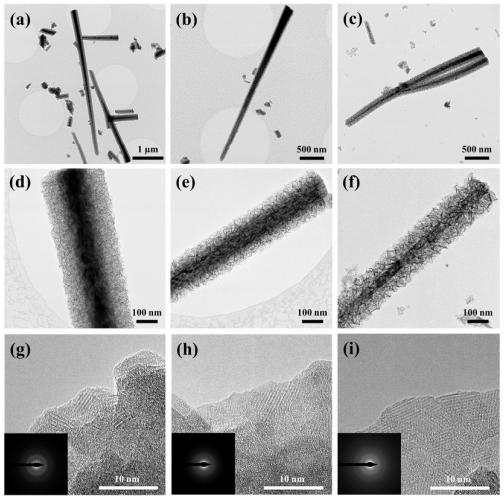

Fig. 3. TEM images of manganese oxide nanorods scratched from the as-synthesized monolithic cordierite substrate for (a) & (d) NA-$CuMn_2O_4$, (b) & (e) NA-$Co_{0.36}Cu_{0.64}Mn_2O_4$, and (c) & (f) NA-$Co_{0.53}Cu_{0.47}Mn_2O_4$, and (g)-(i) the high magnification and insets of electron diffraction analysis, respectively.

Table 2. Average Weight (W, g/L), loading percentages (%) of active materials, and Brunauer–Emmett–Teller (BET) surface areas (SA, m^2/g)

Sample ID	Support type	Average W of monolith catalysts (g/L)	W% of materials loading on monolithic substrates (%) [a]			SA of monolithic catalysts (m^2/g)	SA of MO removed substrates (m^2/g)	Calculated SA of active materials (m^2/g)
			$CuMn_2O_4$	Support	Total			
Cordierite substrate[c]	-		-	-	-	0.5	-	-
HM-PCR core	-	492	-	-	15	36	40	10
NA-$CuMn_2O_4$	NA-PCR	596	12	15	27	35	35	63
NA-$Co_{0.36}Cu_{0.64}Mn_2O_4$	NA-PCR	612	9	13	22	37	31	126
NA-$Co_{0.53}Cu_{0.47}Mn_2O_4$	NA-PCR	564	9	9	18	43	27	218
α-Al_2O_3 powder[c]	-	-	-	-		-	-	26
WC-$CuMn_2O_4$	α-Al_2O_3	808	8	31	39	12	-	46
WC-$Co_{0.36}Cu_{0.64}Mn_2O_4$	α-Al_2O_3	852	8	34	42	15	-	75
WC-$Co_{0.53}Cu_{0.47}Mn_2O_4$	α-Al_2O_3	806	8	31	39	17	-	113

[a] All MnO_2 and $CuMn_2O_4$ materials were removed by aqueous oxalic acid solution.

[b] The - entries signify not applicable or measured.

[c] Commercial products.

The transmission electron microscopy (TEM) images in Figs. 3(a) – 3(c) show that all three $CuMn_2O_4$ coatings are composed of tiny nanosheets uniformly grown on the nanorod surfaces of HM-PCR. Figs. 3(d) – 3(f) reveal the material morphologies affected by the doping of Co ions into the $CuMn_2O_4$ coatings. Obviously, the average size of the $CuMn_2O_4$ nanosheets increases with the higher concentration of Co (Fig. S3). The insets of selected area diffraction patterns (SAED) showing dim amorphous ring patterns confirmed the low crystallinity of all three $CuMn_2O_4$ coatings, which correlate with the low intensities of XRD patterns in Fig. 2(a). Elemental mapping conducted by energy-dispersive X-ray spectroscopy (EDS) shows well-dispersed Mn, Cu, and Co on the three $CuMn_2O_4$ and Co-doped $CuMn_2O_4$ coatings (Fig. S4).

ICP-MS tests were conducted to analyze the elemental ratios between Cu and Mn of copper manganese oxides, which are listed in Table 1. The Cu to Mn ratio of undoped copper manganese oxide (NA-$CuMn_2O_4$) was closed to 1:2, which identifies its chemical formula as $CuMn_2O_4$. For the two Co-doped $CuMn_2O_4$ materials, the percentage of Cu decreased dramatically with increasing Co ion concentration, but with slight Mn change. The detected Co ion concentration in NA-$Co_{0.36}Cu_{0.64}Mn_2O_4$ and NA-$Co_{0.53}Cu_{0.47}Mn_2O_4$ is almost ten times the designed doping ratios, showing that the Co-O-Mn was preferred to be formed during the hydrothermal reaction rather than Cu-O-Mn. These observations are in consistence with earlier reports that Co^{2+} would replace Cu^{2+} in tetrahedral sites and Co^{3+} substituting Mn^{3+} in octahedral sites of the $CuMn_2O_4$ lattice.[44]

Table 2 summarizes the weight loading percentages and surface areas (SA) of both nanoarray-based and wash-coated monolithic catalysts. The nanoarray-based monolithic catalysts have relatively higher surface areas (35-43 m^2/g) than the wash-coated monolithic catalysts (12-17 m^2/g). Overall, all $CuMn_2O_4$ based monolithic catalysts show a trend of increasing surface area with increasing Co doping. Furthermore, both nanoarray-based and wash-coated monolithic catalysts have partial surface area contributed by their supporting materials, MnO_2 nanoarrays (HM-PCR) core, and α-Al_2O_3, respectively. The main substrate, cordierite honeycomb monoliths, is partially etched by acid during the hydrothermal synthesis of HM-PCR fabrication.[27] Therefore, the surface areas of the nanoarray-based and wash-coated monolithic catalysts were subtracted from the surface area of core supports and uncoated substrates (cordierite) using Equations 1 and 2 correspondingly, to obtain the recalculated surface area of $CuMn_2O_4$ coatings and powders.

$$S_{CMO} = \frac{S_M \times W_M - S_{BC} \times W_{BC} - S_{PCR} \times W_{PCR}}{W_{CMO}} \quad (1)$$

$$S_{WC} = \frac{S_M \times W_M - S_{BC} \times W_{BC} - S_{AlO} \times W_{AlO}}{W_{WC}} \quad (2)$$

In Equations 1 and 2, S_{CMO} and W_{CMO} are the surface areas and weights of $CuMn_2O_4$ material coatings on the HM-PCR core nanoarrays, respectively; S_{WC} and W_{WC} are used for the wash-coated monolithic catalysts; S_M and W_M are used for the whole monolithic catalysts; S_{BC} and W_{BC} refer to the uncoated cordierite substrate; S_{PCR} and W_{PCR} refer to the core nanoarrays, HM-PCR; S_{AlO} and W_{AlO} refer to the α-Al_2O_3 support powder.

After subtraction of core supports and cordierite substrates, the recalculated surface area of the $CuMn_2O_4$ coatings showed the same trend as monolithic catalysts, NA-$Co_{0.53}Cu_{0.47}Mn_2O_4$ > NA-$Co_{0.36}Cu_{0.64}Mn_2O_4$ > NA-$CuMn_2O_4$, but the surface areas of the $CuMn_2O_4$ coating on nanoarray-based monolithic catalysts are much higher than the $CuMn_2O_4$ powders used for the wash-coated monolithic catalysts, i.e. NA-$Co_{0.53}Cu_{0.47}Mn_2O_4$ (218 m^2/g) > WC-$Co_{0.53}Cu_{0.47}Mn_2O_4$ (113 m^2/g). Correlating the surface areas to their morphologies in Fig. 3 reveals that the $CuMn_2O_4$ coatings on nanoarray architectures can maintain high surface area [Figs. 3(d)-(f)] and avoid/mitigate aggregation.

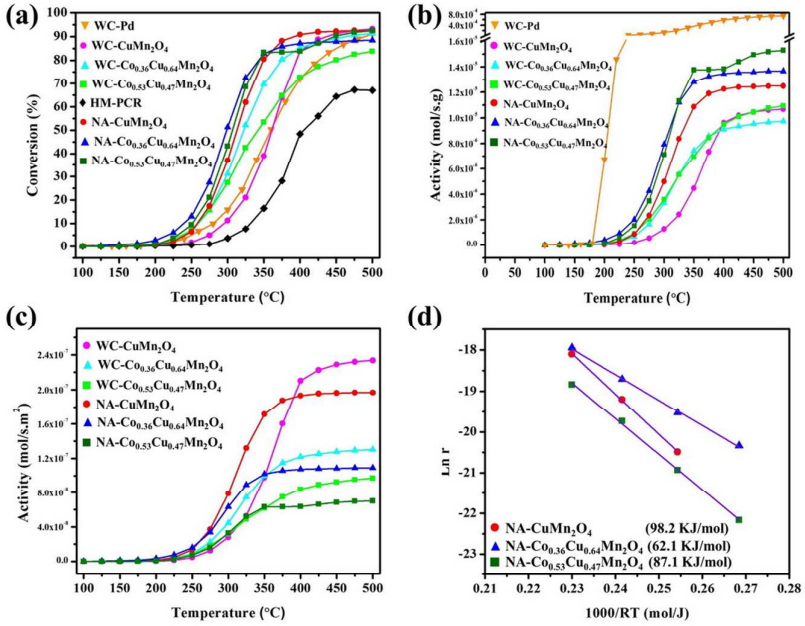

Fig. 4. (a) Catalytic performance of nanoarray-based and wash-coated monolithic catalysts for C_3H_8 oxidation; (b) the calculated activities as a function of temperature; (c) the calculated activities normalized by surface area as a function of temperature; (d) the Arrhenius plot of the reaction kinetics and the calculated apparent activation energies.

3.2 Catalytic propane oxidation behavior

The catalytic performance of the $CuMn_2O_4$ coated nano-array based and wash-coated monolithic catalysts were studied using oxidation of propane (C_3H_8) as shown in Fig. 4(a) in comparison with a Pd/α-Al_2O_3 wash-coated monolithic catalyst. In general, catalytic performance varied with the feed gas rate. Fig. S5 shows both the light-off temperature (T_{50}) and the 90% conversion temperature (T_{90}) of NA-$CuMn_2O_4$ are directly proportional to the feed gas rate. Then, we simply used 100 SCCM gas rate and space velocity of 24,000 h^{-1} for each C_3H_8 oxidation test. Overall, the nanoarray-based monolithic catalysts showed better catalytic performance than both Pd and wash-coated $CuMn_2O_4$ monolithic catalysts. All the three nanoarray-based monolithic catalysts, NA-$CuMn_2O_4$, NA-$Co_{0.36}Cu_{0.64}Mn_2O_4$, and NA-$Co_{0.53}Cu_{0.47}Mn_2O_4$ possessed good reactivity with light-off temperature (T_{50}) around 300°C, 25 °C lower than the wash-coated catalysts, WC-$Co_{0.36}Cu_{0.64}Mn_2O_4$ (325 °C) and 50 °C lower than WC-$CuMn_2O_4$ and the Pd loaded catalyst, WC-Pd (350 °C). Among the three nanoarray-based monolithic catalysts, the NA-$CuMn_2O_4$ presented the higher reactivity to C_3H_8 oxidation and T_{90} at 400 °C, which was 50 °C lower than the Co-doped catalysts. The NA-$Co_{0.36}Cu_{0.64}Mn_2O_4$ and NA-$Co_{0.53}Cu_{0.47}Mn_2O_4$ showed better performance than the NA-$CuMn_2O_4$ below 350 °C.

For the series of wash-coated monolithic catalysts, the $CuMn_2O_4$ powders loaded catalyst also revealed higher activity than the Pd loaded catalyst. WC-$CuMn_2O_4$ has similar T_{50} (360 °C) but lower T_{90} (450 °C) as compared to WC-Pd (T_{50} ~ 360 °C, T_{90} ~ 500 °C). Similar to the nano-array based catalysts, Co doping also increases the reactivity of wash-coated $CuMn_2O_4$ catalysts in the lower temperature region and reach 50% conversion at 325 °C.

Comprehensively, the nanoarray-based catalysts have better catalytic performance and lower T_{90} at around 400 °C than the wash-coated catalysts, WC-$CuMn_2O_4$ (450 °C), WC-$Co_{0.36}Cu_{0.64}Mn_2O_4$ (475 °C), and WC-Pd (475 °C).

Due to different precipitation rates and the loading ratio of $CuMn_2O_4$ from hydrothermal synthesis and wash-coating process, the comparison of reactivity among monolithic catalysts was normalized by loading weight as shown in Fig. 4(b). After normalization using the exact coating weight, the wash-coated Pd catalyst, WC-Pd, exhibits better activity than all $CuMn_2O_4$-coated monolithic catalysts. For the nanoarray-based catalysts, the order of normalized activity is NA-$Co_{0.53}Cu_{0.47}Mn_2O_4$ > NA-$Co_{0.36}Cu_{0.64}Mn_2O_4$ > NA-$CuMn_2O_4$. Each $CuMn_2O_4$ coated nanoarray-based catalysts still possessed higher activity than their wash-coated counterparts, which proved that the nanoarray structure benefit to the catalytic performance of C_3H_8 oxidations.

For further comparison among the $CuMn_2O_4$ and Co-doped $CuMn_2O_4$ materials, their activities were normalized simultaneously with both surface area and active material loading weight as shown in Fig. 4(c). A reversed order of the normalized activities, NA-$CuMn_2O_4$ > NA-$Co_{0.36}Cu_{0.64}Mn_2O_4$ > NA-$Co_{0.53}Cu_{0.47}Mn_2O_4$, indicates the significance of surface area contributing to the oxidation reactivity. The slight Co dopping efficiently increases the surface area of $CuMn_2O_4$ materials and promotes their catalytic performance in this study.

Fig. 4(d) presents the calculated activation energies of the three nanoarray-based monolithic catalysts in the Arrhenius plot with the order, NA-$Co_{0.36}Cu_{0.64}Mn_2O_4$ (62.1 KJ/mol) < NA-

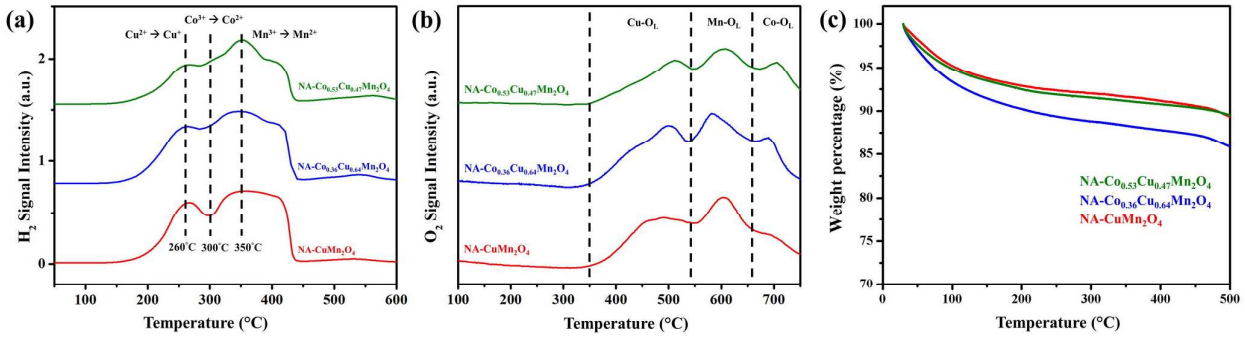

Fig. 5. (a) H_2-TPR and (b) O_2-TPD profiles of monolithic catalysts, NA-$CuMn_2O_4$, NA-$Co_{0.36}Cu_{0.64}Mn_2O_4$, and NA-$Co_{0.53}Cu_{0.47}Mn_2O_4$. (c) Thermogravimetric analysis (TGA) of coating materials, $CuMn_2O_4$, $Co_{0.36}Cu_{0.64}Mn_2O_4$, and$Co_{0.53}Cu_{0.47}Mn_2O_4$ collected from each hydrothermal reaction.

$Co_{0.53}Cu_{0.47}Mn_2O_4$ (87.1 KJ/mol) < NA-$CuMn_2O_4$ (98.2 KJ/mol). $CuMn_2O_4$ possesses lower activation energies with the incorporation of cobalt ions. The 1% Co-doped catalyst shows the lowest activation energy among all catalysts, which agreed with its lowest light-off temperature (~300°C) as shown in Fig. 4(a).

3.3 Temperature programmed reduction and desorption characteristics

Hydrogen temperature programmed reduction (H_2-TPR) was conducted to study the effect of cobalt ion doping on the reducibility of $CuMn_2O_4$ based catalysts. In Fig. 5(a), the H_2-TPR profile of NA-$CuMn_2O_4$ shows two typical consecutive peaks at around 260 °C and 350 °C that are consistent with the results of Jones et al. and Cai et al. which can be attributed to the reduction of Cu^{2+} → Cu^{+} and Mn^{3+} → Mn^{2+}, respectively.[44, 45] The broadened reduction peaks compared to those results are due to the open channel configuration of monolithic samples. In the TPR profiles of both two Co-doped catalysts, the reduction of cobalt ions (Co^{3+} → Co^{2+}) slightly changed the profile shape of $CuMn_2O_4$ and led to the diminished troughs around 300 °C and small humps around 350 °C. With Co doping, NA-$Co_{0.36}Cu_{0.64}Mn_2O_4$ and NA-$Co_{0.53}Cu_{0.47}Mn_2O_4$ showed relatively lower starting temperatures in H_2-TPR tests, which followed the same tendency as their activation energies, NA-$Co_{0.36}Cu_{0.64}Mn_2O_4$ < NA-$Co_{0.53}Cu_{0.47}Mn_2O_4$ < NA-$CuMn_2O_4$.

The nature of oxygen species in coated $CuMn_2O_4$ materials was investigated using oxygen temperature programmed desorption (O_2-TPD) experiments. Overall, the three catalysts had similar starting temperatures of oxygen evolution around 350 °C. Between 350-750 °C, each O_2-TPD profile can be separated into three regions: (I) 350-540 °C, (II) 540-660 °C, and (III) 660-750 °C, according to the major desorption peaks. In Fig. 5(b), the TPD profile of $CuMn_2O_4$ only shows two oxygen desorption peaks in regions I and II, which belong to the bulk lattice oxygen evolution from metal-oxygen bonding, Cu-O_L and Mn-O_L. But the TPD profiles of the two Co-doped $CuMn_2O_4$ catalysts show clear desorption peaks in region III indicating oxygen evolution from Co-O_L bonding. The relative intensities of desorption peaks in region I and region III also varied with the change of Cu and Co ratio in the catalysts NA-$Co_{0.36}Cu_{0.64}Mn_2O_4$ and NA-$Co_{0.53}Cu_{0.47}Mn_2O_4$. For example, from the ICP test, the elemental component of NA-$Co_{0.53}Cu_{0.47}Mn_2O_4$ catalyst possesses less copper but more cobalt compared to the NA-$Co_{0.36}Cu_{0.64}Mn_2O_4$ catalyst, and the O_2-TPD profile simultaneously shows a lower intensity peak in region I and a higher peak in region III. This phenomenon agrees with the study of Morales et al., which presented an analogous result of the varied ratio between Cu and Mn in Mn_xCu_y mixed oxides.[46] These results also demonstrate that the three regions of lattice oxygen evolution in our O_2-TPD profiles can be distinguished as follows, (i) region I (350-540 °C): Cu-O_L, (ii) region I (540-660 °C): Mn-O_L, and (iii) region I (660-750 °C): Co-O_L.

3.4 Thermal analysis and stability of catalysts

Thermogravimetric analysis (TGA) of the powder-form $CuMn_2O_4$ materials collected from respective hydrothermal synthesis are shown in Fig. 5(c) with sample weight percentages as a function of temperature. The TGA profiles show a 6~8% weight loss before 100 °C by the release of physisorbed water molecules. As shown in the O_2-TPD study [Fig. 5(b)], the evolution of lattice oxygen starts with heating up to 350 °C. An obvious decay around 450 °C should be due to the crystal phase formation of hopcalite $CuMn_2O_4$ and phase segregation of MnO_2 according to the XRD patterns at high temperature as shown in Figs. 2(b)-(d). $Co_{0.36}Cu_{0.64}Mn_2O_4$ shows more weight loss as compared to $CuMn_2O_4$ and $Co_{0.53}Cu_{0.47}Mn_2O_4$ indicating the lower thermal stability among the three materials.

3.5 Surface composition and oxidation state

X-ray photoelectron spectroscopy (XPS) was used to obtained detailed valence states of the major component in the surfaces of catalysts. The XPS spectra in Fig. 6 illustrate the surface elemental compositions of the powder collected from hydrothermal coating synthesis of NA-$CuMn_2O_4$, NA-$Co_{0.36}Cu_{0.64}Mn_2O_4$, and NA-$Co_{0.53}Cu_{0.47}Mn_2O_4$. All binding energies (BEs) and elemental ratios correspond to the peaks of Mn 2p, Cu 2p, Co 2p, and O 1s and are summarized in Table 3. In Fig. 6(a), the Mn $2p_{3/2}$ peaks at around 641 eV indicate the Mn^{3+} as the major Mn in each $CuMn_2O_4$ material.[39] The Cu 2p spectra in Fig. 6(b) are characterized by the peaks of Cu $2p_{3/2}$ (932 eV) and Cu $2p_{1/2}$ (952 eV), and observable satellite peaks

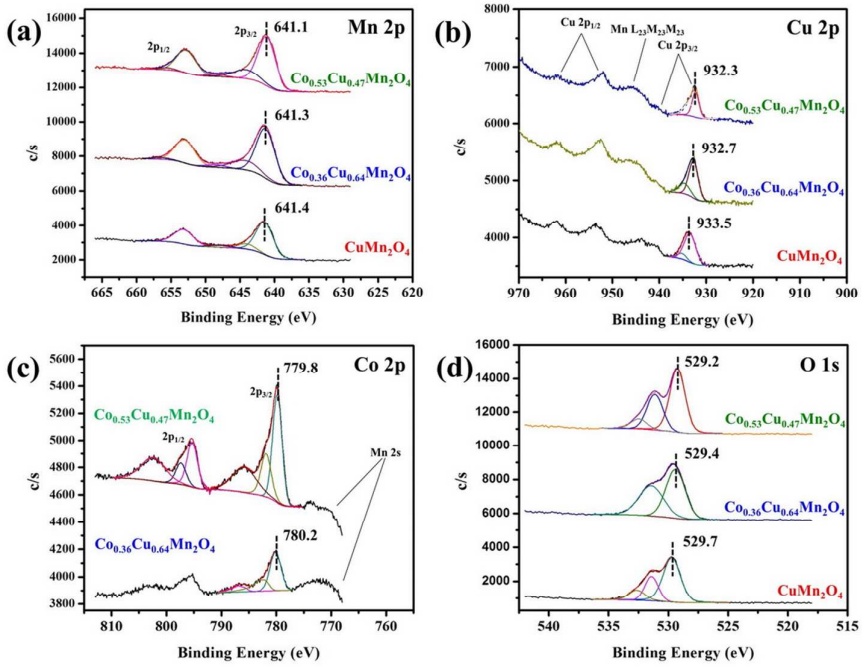

Fig. 6. X-ray photoelectron spectroscopy (XPS) analysis of (a) Mn 2p, (b) Cu 2p, (c) Co 2p, and (d) O 1s of $CuMn_2O_4$, $Co_{0.36}Cu_{0.64}Mn_2O_4$, and $Co_{0.53}Cu_{0.47}Mn_2O_4$ collected from each hydrothermal reaction.

Table 3. Summary of Binding Energies (BEs) of Cu, Mn, Co, and O from the XPS Spectra

Sample ID	Binding Energy (eV)							
	Mn $2p_{3/2}$ (%)		Cu $2p_{3/2}$	Co $2p_{3/2}$ (%)		O 1s (%)		
	Mn^{4+}	Mn^{3+}	Cu^{2+}	Co^{2+}	Co^{3+}	O_{OH}	O_{ads}	O_L
NA-$CuMn_2O_4$	644.0 (14.8)	641.0 (85.2)	933.5	-	-	532.6 (13.7)	531.4 (24.1)	529.7 (62.2)
NA-$Co_{0.36}Cu_{0.64}Mn_2O_4$	644.2 (23.7)	641.3 (76.3)	932.7	782.2 (31.7)	780.2 (68.3)	-	531.4 (45.4)	529.4 (54.6)
NA-$Co_{0.53}Cu_{0.47}Mn_2O_4$	644.1 (23.1)	641.1 (76.9)	932.3	781.9 (32.4)	779.8 (67.6)	532.5 (9.4)	531.1 (32.1)	529.2 (58.5)

The - entries signify not applicable or measured.

at around 940 eV and 962 eV, which correspond to Cu^{2+}; with no obvious peaks from Cu^0 and Cu^+ detected.[47, 48] In Fig. 6(c), the respective Co $2p_{3/2}$ and Co $2p_{1/2}$ peaks at around 780 eV and 795 eV are accompanied with satellite peaks at 786 eV and 806 eV due to the majority of Co^{2+}.[48] Detectable shoulders at around 782 eV indicate the minor existence of Co^{3+} in the catalysts. The Shirley function was not applied to correct the background of Cu 2p and Co 2p spectra because of the overlap of Mn LMM (945 eV) and Mn 2s peaks (772 eV), respectively. The O 1s spectra in Fig. 6(d) can be de-convoluted to two or three Gaussian peaks associated with lattice oxygen (O_L, 529.4 eV), surface-adsorbed oxygen species (O_{ads}, 531.4 eV, i.e. O_2^-, O_2^{2-}, and O^-), and surface adsorbed OH groups and molecular water (O_{OH}, 532.5 eV, i.e. OH^- and H_2O).[39]

4. Discussion

4.1 Synthesis and morphologies

The cryptomelane MnO_2 nanoarray HM-PCR, synthesized using manganese sulfate ($MnSO_4$) and potassium chlorate ($KClO_3$), was chosen as the core support due to the high length-to-diameter ratio (average lengths of 5 μm and diameters of 50 nm). The appropriate interspaces between the rods provide enough room for the growth of $CuMn_2O_4$ layers without sacrificing active surface. Additional advantages, like the simple synthetic procedure, potential scalability, high robustness, and good stability in hydrothermal reactions ensure that nanoarray HM-PCR has no influence on the

secondary transitional metal oxide coatings during the synthesis.

The mild conditions of the hydrothermal $CuMn_2O_4$ coating, e.g. neutral solution, low temperature, and slow precipitation rate, contribute to the uniform and tunable thickness of $CuMn_2O_4$ layers from top to bottom along the whole HM-PCR nanoarrays. The introduction of cobalt ions accelerate the precipitation rate to obtain the same thickness of coating layers in a shorter reaction time. Correlating the elemental ratio between Co and Cu ions in NA-$Co_{0.36}Cu_{0.64}Mn_2O_4$ and NA-$Co_{0.53}Cu_{0.47}Mn_2O_4$ from ICP-MS tests (Table 1), Co ions replace the Cu ions in the $CuMn_2O_4$ system due to the more energetically favorable formation of Co-O bonds (ΔH_f = 368 KJ/mol) than Cu-O bonds (ΔH_f = 343 KJ/mol), which results in more Co in the materials than expected.

Comparing the supporting types and preparation methods, nanoarray-based catalysts have less average weight (~ 600 g/L) of unit monolithic size than wash-coated catalyst (~ 800 g/L). nanoarray-based catalysts also have less weight percentage of the core nanoarrays (9 – 15%) but higher surface area (35 – 43 m^2/g) compared to the wash-coated catalysts with alumina powder support (SA: 12 – 17 m^2/g, loading: 31 – 34%).[4943]

In addition, the calculated SA of NA-$Co_{0.53}Cu_{0.47}Mn_2O_4$ from the nanoarray-based catalyst (218 m^2/g) is almost double that of WA-$Co_{0.53}Cu_{0.47}Mn_2O_4$ (113 m^2/g). This result indicated that the core nanoarrays (HM-PCR) provide a useful support for $CuMn_2O_4$ coating layers preventing material aggregation and efficiently maintaining high surface area, and maximizing active sites.

4.2 Catalytic performance

Propane (C_3H_8) oxidations were conducted to evaluate the catalytic performance of all nanoarray-based and wash-coated monolithic catalysts as shown in Fig. 4. The Pd/Al_2O_3 wash-coated catalyst (WC-Pd) was used as a state-of-art monolithic catalyst to compare with our $CuMn_2O_4$ coated catalysts. In Fig. 4(a), all $CuMn_2O_4$ based monolithic catalysts exhibit lower light-off temperatures (T_{50}) and 90% conversion temperatures (T_{90}) than the Pd loaded catalyst, WC-Pd, indicating the high reactivity to hydrocarbons of the $CuMn_2O_4$ coatings.

In general, nanoarray-based monolithic catalysts possess open surfaces of nanoarray architectures with exposure to more sufficient active sites than traditional wash-coated monolithic catalysts. The promoted activities by the open surfaces of nanoarrays were examined by comparing the normalized activities of nanoarray-based and wash-coated catalysts shown in Fig. 4(b). All the three nanoarray-based catalysts reveal higher activities of C_3H_8 oxidation than each correlated wash-coated monolithic catalyst after normalization with loading weight. This result indicates that the $CuMn_2O_4$ nanosheet coatings on nanoarrays lead to better mass transfer during C_3H_8 oxidations than mixing with α-Al_2O_3 powder. Furthermore, the order of weight normalized activities for the three nanoarray-based catalysts (NA-$Co_{0.53}Cu_{0.47}Mn_2O_4$ > NA-$Co_{0.36}Cu_{0.64}Mn_2O_4$ > NA-$CuMn_2O_4$) became reversed after normalization with material surface area, which demonstrates the largely increased surface area of $CuMn_2O_4$ nanosheets by Co doping contributing to high catalytic activities. Among the nanoarray-based catalysts, the order of reactivity is NA-$Co_{0.53}Cu_{0.47}Mn_2O_4$ ~ NA-$Co_{0.36}Cu_{0.64}Mn_2O_4$ > NA-$CuMn_2O_4$, as the same tendency as the wash-coated catalysts. The two Co-doped catalysts present similar reactivity but are higher than the pure $CuMn_2O_4$ catalyst below 350 °C showing the enhanced reactivity by the incorporation of Co ions in the low-temperature region.[50]

The calculated activation energies (E_a) are listed in Fig. 4(d) with the increasing order NA-$Co_{0.36}Cu_{0.64}Mn_2O_4$ (62.1 KJ/mol) < NA-$Co_{0.53}Cu_{0.47}Mn_2O_4$ (87.1 KJ/mol) < NA-$CuMn_2O_4$ (98.2 KJ/mol). This result shows the same tendency with the study of Salker et al. in 2000 that $Co_xCu_{1-x}Mn_2O_4$ catalysts were tested with varied Co/Cu ratios (x = 0.0, 0.3, 0.5, 0.7, and 1.0).[51] And the catalytic performance of CO oxidations indicates the catalysts with x = 0.3 and 0.7 show a relatively higher reactivity than catalysts with x = 0.0, 0.5, and 1.0. Correlating the activation energies of nanoarray-based catalysts to our H_2-TPR and O_2-TPD results, the additional reduction peak of Co ions ($Co^{3+} \rightarrow Co^{2+}$) and lower evolution temperature of lattice oxygen (Mn-O_L) respectively contribute to higher reducibility and oxygen mobility and lower E_a of Co-incorporated catalysts.

4.3 Oxidation States

The XPS study reveals the oxidation states of metal elements near the surface, which usually play a significant role influencing the catalytic reactivity. The major oxidation states of Mn, Cu, and Co in the series of $CuMn_2O_4$ are determined as Mn^{3+}, Cu^{2+}, and Co^{2+} according to their binding energies (BEs) and corresponding satellite peaks as shown in Figs. 6(a)-(c). The BEs of Mn, Cu, and O for all catalysts decrease with increasing contents of Co suggesting that the incorporation of Co might enhance the mobility of lattice oxygen.

For the two Co-doped catalysts, $Co_{0.36}Cu_{0.64}Mn_2O_4$ and $Co_{0.53}Cu_{0.47}Mn_2O_4$, the existence of Mn LMM peaks (~944.1 eV) in Cu 2p spectra [(Fig. 6(b)] and Mn 2s peaks (~768.6 eV) in Co 2p spectra [(Fig. 6(c)] cause some difficulty to distinguish the precise composition of Cu $2p_{3/2}$ and Co $2p_{3/2}$ peaks. However, as shown in Fig. 6(c), the intensity of the Mn 2s signal observed from $Co_{0.36}Cu_{0.64}Mn_2O_4$ is relatively higher than $Co_{0.53}Cu_{0.47}Mn_2O_4$ indicating the higher surface concentration of Mn in $Co_{0.36}Cu_{0.64}Mn_2O_4$.

In Fig. 6(d), the O 1s peak of $Co_{0.36}Cu_{0.64}Mn_2O_4$ can only be de-convoluted into two well-fitting Gaussian peaks for lattice oxygens and surface-adsorbed oxygen species rather than three peaks as shown in $CuMn_2O_4$ and $Co_{0.53}Cu_{0.47}Mn_2O_4$. This result suggests that the $Co_{0.36}Cu_{0.64}Mn_2O_4$ material has trace surface adsorbed hydroxyl species (OH^-) and molecular water but a relatively higher percentage of surface-adsorbed oxygen species (O_{ads}, 45.4%), which are usually considered as better catalytic oxidation promoters, than the other two catalysts.

Correlating the E_a of each catalyst to the XPS analysis, the order of O_{ads} percentages in catalysts, $Co_{0.36}Cu_{0.64}Mn_2O_4$ (45.4%) > $Co_{0.53}Cu_{0.47}Mn_2O_4$ (32.1%) > $CuMn_2O_4$ (24.1%), reveals a reversed tendency of activation energies presented in Fig. 4(d), $Co_{0.36}Cu_{0.64}Mn_2O_4$ (62.1 KJ/mol) < $Co_{0.53}Cu_{0.47}Mn_2O_4$ (87.1 KJ/mol) < $CuMn_2O_4$ (98.2 KJ/mol).

Overall, the lower E_a of Co-doped $CuMn_2O_4$ than the pure $CuMn_2O_4$ is due to the higher concentrations of Mn and O_{ads} near the material surface. The highest amounts of Mn^{4+}, O_{ads}, and negligible O_{OH} lead to the lowest E_a of $Co_{0.36}Cu_{0.64}Mn_2O_4$.

5. Conclusions

Advanced nanoarray-based monolithic catalysts were successfully fabricated by coating $CuMn_2O_4$ nanosheets onto the HM-PCR nanoarrays. The synthetic process exhibits good hydrothermal durability and loading capability of HM-PCR nanoarrays for additional transitional metal oxide layers. The composite monolithic catalysts combine the high reactivity of $CuMn_2O_4$ materials and open surface efficacy of nanoarray architecture to provide better catalytic performance for C_3H_8 oxidation. Compared to wash-coated catalysts, nanoarrays are able to replace alumina supports and efficiently reduce the integrated weight of monolithic catalysts. The incorporation of cobalt ions effectively increases the specific surface area from 63 m^2/g to 218 m^2/g, and lowers the apparent activation energy from 98.2 KJ/mol to 62.1 KJ/mol with compromised thermal stability. XPS studies show that the NA-$Co_{0.36}Cu_{0.64}Mn_2O_4$ catalyst possesses a higher surface concentration of Mn and surface-adsorbed oxygen, which contribute to the highest catalytic performance observed in this study. Different from traditional hydrothermal syntheses, all procedures were conducted in an open system reactor at atmospheric pressure revealing the potential for scalability for industrial manufacturing processes.

Conflicts of interest

The authors declare no conflicts to declare.

Acknowledgements

Funding for this research was provided by National Science Foundation (NSF) under NSF grant # CBET-1344792. The authors also acknowledge use of the microscopy supported by NSF grant #: 1126100 in the Biosciences Electron Microscopy Facility of the University of Connecticut and assistance from Dr. Xuanhao Sun. The authors thank Dr. Bill Willis for XPS experiments and Dr. Frank Galasso for helpful discussions and suggestions.

Notes and references

1. *UNEP Year Book 2014 emerging issues update - Air Pollution: World's Worst Environmental Health Risk*, United Nations Environment Programme, 2014.
2. *Adoption of the Paris Agreement*, UNFCCC. Conference of the Parties (COP), 2015.
3. J. A. Pihl, R. Blint and C. S. Daw, *2015 CLEERS Industry Priorities Survey Final Report*, U.S. Department of Energy, Advanced Engine Cross-Cutting Technology Development Team, 2016.
4. R. J. Farrauto, M. Hobson, T. Kennelly and E. Waterman, *Appl. Catal., A*, 1992, **81**, 227-237.
5. S. Salasc, M. Skoglundh and E. Fridell, *Appl. Catal., B*, 2002, **36**, 145-160.
6. C.-H. Kim, S. I. Woo and S. H. Jeon, *Ind. Eng. Chem. Res.*, 2000, **39**, 1185-1192.
7. W. Tang, W. Xiao, S. Wang, Z. Ren, J. Ding and P.-X. Gao, *Appl. Catal., B*, 2018, **226**, 585-595.
8. W. Song, A. S. Poyraz, Y. Meng, Z. Ren, S.-Y. Chen and S. L. Suib, *Chem. Mater.*, 2014, **26**, 4629-4639.
9. J. S. Yang, W. Y. Jung, G. D. Lee, S. S. Park, E. D. Jeong, H. G. Kim and S.-S. Hong, *J. Ind. Eng. Chem.*, 2008, **14**, 779-784.
10. H. Yao and Y. Y. Yao, *J. Catal.*, 1984, **86**, 254-265.
11. G. G. Xia, Y. G. Yin, W. S. Willis, J. Y. Wang and S. Suib, *J. Catal.*, 1999, **185**, 91-105.
12. C. H. Kim, G. Qi, K. Dahlberg and W. Li, *Science*, 2010, **327**, 1624-1627.
13. Y. Nishihata, J. Mizuki, T. Akao, H. Tanaka, M. Uenishi, M. Kimura, T. Okamoto and N. Hamada, *Nature*, 2002, **418**, 164-167.
14. T. M. Onn, M. Monai, S. Dai, E. Fonda, T. Montini, X. Pan, G. W. Graham, P. Fornasiero and R. J. Gorte, *J. Am. Chem. Soc.*, 2018, **140**, 4841-4848.
15. S. Cai, J. Liu, K. Zha, H. Li, L. Shi and D. Zhang, *Nanoscale*, 2017, **9**, 5648-5657.
16. Y. Liu, J. Xu, H. Li, S. Cai, H. Hu, C. Fang, L. Shi and D. Zhang, *J. Mater. Chem. A*, 2015, **3**, 11543-11553.
17. L. Huang, X. Zhao, L. Zhang, L. Shi, J. Zhang and D. Zhang, *Nanoscale*, 2015, **7**, 2743-2749.
18. K. Li, M. Ma, L. Xie, Y. Yao, R. Kong, G. Du, A. M. Asiri and X. Sun, *Int. J. Hydrogen Energy*, 2017, **42**, 19028-19034.
19. H.-J. Lin, J. P. Baltrus, H. Gao, Y. Ding, C.-Y. Nam, P. Ohodnicki and P.-X. Gao, *ACS Appl. Mater. Interfaces*, 2016, **8**, 8880-8887.
20. Y. Guo, Z. Ren, W. Xiao, C. Liu, H. Sharma, H. Gao, A. Mhadeshwar and P.-X. Gao, *Nano Energy*, 2013, **2**, 873-881.
21. Z. Ren, V. Botu, S. Wang, Y. Meng, W. Song, Y. Guo, R. Ramprasad, S. L. Suib and P. X. Gao, *Angew. Chem. Int. Ed.*, 2014, **53**, 7223-7227.
22. S. Hoang and P. X. Gao, *Adv. Energy Mater.*, 2016, **6**, 1600683.
23. S. Du, S. Wang, Y. Guo, X. Lu, W. Tang, Y. Ding, X. Mao and P.-X. Gao, *Appl. Catal., B*, 2018, **236**, 348-358.
24. W. Tang, Z. Ren, X. Lu, S. Wang, Y. Guo, S. Hoang, S. Du and P.-X. Gao, *ChemCatChem*, 2017, **9**, 4112-4119.
25. S. Wang, Z. Ren, Y. Guo and P.-X. Gao, *CrystEngComm*, 2016, **18**, 2980-2993.
26. S. Wang, Z. Ren, W. Song, Y. Guo, M. Zhang, S. L. Suib and P.-X. Gao, *Catal. Today*, 2015, **258**, 549-555.
27. S.-Y. Chen, W. Song, H.-J. Lin, S. Wang, S. Biswas, M. Mollahosseini, C.-H. Kuo, P.-X. Gao and S. L. Suib, *ACS Appl. Mater. Interfaces*, 2016, **8**, 7834-7842.
28. H. Chen, J. Wang, H. Li, D. Wu, M. Yao and Y. Li, *Appl. Catal., A*, 2012, **427**, 73-78.
29. A. A. Mirzaei, H. R. Shaterian, R. W. Joyner, M. Stockenhuber, S. H. Taylor and G. J. Hutchings, *Catal. Commun.*, 2003, **4**, 17-20.

30. W. Tang, X. Wu, S. Li, X. Shan, G. Liu and Y. Chen, *Appl. Catal., B*, 2015, **162**, 110-121.
31. Z. Ye, J. M. Giraudon, N. Nuns, P. Simon, N. De Geyter, R. Morent and J. F. Lamonier, *Appl. Catal., B*, 2018, **223**, 154-166.
32. G. J. Hutchings, A. A. Mirzaei, R. W. Joyner, M. R. H. Siddiqui and S. H. Taylor, *Catal. Lett.*, 1996, **42**, 21-24.
33. Y. Hasegawa, K. Fukumoto, T. Ishima, H. Yamamoto, M. Sano and T. Miyake, *Appl. Catal., B*, 2009, **89**, 420-424.
34. S. A. Kondrat, T. E. Davies, Z. Zu, P. Boldrin, J. K. Bartley, A. F. Carley, S. H. Taylor, M. J. Rosseinsky and G. J. Hutchings, *J. Catal.*, 2011, **281**, 279-289.
35. S. Vepřek, D. Cocke, S. Kehl and H. Oswald, *J. Catal.*, 1986, **100**, 250-263.
36. Z. Jaworska-Galas, W. Mista, J. Wrzyszcz and M. Zawadzki, *Catal. Lett.*, 1994, **24**, 133-139.
37. G. Fortunato, H. Oswald and A. Reller, *J. Mater. Chem.*, 2001, **11**, 905-911.
38. D. Cocke and S. Vepřek, *Solid State Commun.*, 1986, **57**, 745-748.
39. H. Zhao, K. Fang, J. Zhou, M. Lin and Y. Sun, *Int. J. Hydrogen Energy*, 2016, **41**, 8819-8828.
40. B. Faure and P. Alphonse, *Appl. Catal., B*, 2016, **180**, 715-725.
41. J. A. Enterkin, W. Setthapun, J. W. Elam, S. T. Christensen, F. A. Rabuffetti, L. D. Marks, P. C. Stair, K. R. Poeppelmeier and C. L. Marshall, *ACS Catal.*, 2011, **1**, 629-635.
42. Z. Zhu, G. Lu, Z. Zhang, Y. Guo, Y. Guo and Y. Wang, *ACS Catal.*, 2013, **3**, 1154-1164.
43. C. Jones, K. J. Cole, S. H. Taylor, M. J. Crudace and G. J. Hutchings, *J. Mol. Catal. A: Chem.*, 2009, **305**, 121-124.
44. C. Jones, S. H. Taylor, A. Burrows, M. J. Crudace, C. J. Kiely and G. J. Hutchings, *Chem. Commun.*, 2008, **0**, 1707-1709.
45. L. Cai, Z. Hu, P. Branton and W. Li, *Chin. J. Catal.*, 2014, **35**, 159-167.
46. M. R. Morales, B. P. Barbero and L. E. Cadús, *Fuel*, 2008, **87**, 1177-1186.
47. K.-H. Choi, D.-H. Lee, H.-S. Kim, Y.-C. Yoon, C.-S. Park and Y. H. Kim, *Ind. Eng. Chem. Res.*, 2016, **55**, 4443-4450.
48. C. D. Wagner and G. Muilenberg, *Handbook of X-ray photoelectron spectroscopy*, Perkin-Elmer Corp., Physical Electronics Division, Eden Prairie, Minnesota, USA, 1979.
49. Z. Ren, Z. Wu, W. Song, W. Xiao, Y. Guo, J. Ding, S. L. Suib and P.-X. Gao, *Appl. Catal., B*, 2016, **180**, 150-160.
50. H.-J. Lin, J. P. Baltrus, H. Gao, Y. Ding, C. Y. Nam, P. Ohodnicki and P.-X. Gao, *ACS Appl. Mater. Interfaces*, 2016, **8**, 8880-8887.
51. A. Salker and S. Gurav, *J. Mater. Sci.*, 2000, **35**, 4713-4719.